Nuclear Engineering and Technology 56 (2024) 2584–2594

Contents lists available at ScienceDirect

Nuclear Engineering and Technology

journal homepage: www.elsevier.com/locate/net

Original Article

Enhancement of FeCrAl-ODS steels through optimised SPS parameters and addition of novel nano-oxide formers

A. Meza [a,b,*], E. Macía [a], M. Serrano [c], C. Merten [d], U. Gaitzsch [d], T. Weißgärber [d,e], M. Campos [a]

[a] Dpt. Materials Science and Engineering, IAAB, Universidad Carlos III de Madrid (UC3M), Av. de la Universidad 30, 28911, Leganés, Spain
[b] IMDEA Materials Institute, C/ Eric Kandel 2, 28906, Getafe, Spain
[c] Structural Materials Division, Technology Department, CIEMAT, Avda de la Complutense 22, 28040, Madrid, Spain
[d] Fraunhofer Institute for Manufacturing Technology and Advanced Materials IFAM, Dresden, Germany
[e] TUD Dresden University of Technology, Dresden, Germany

ARTICLE INFO

Keywords:
ODS steel
Mechanical alloying
Spark plasma sintering
Zirconium
Co-precipitation
Small punch tests

ABSTRACT

A novel approach to incorporating oxide formers into ferritic ODS production has been developed using the co-precipitation technique. This method enables the tailored design of complex nano-oxides, integrated during Mechanical Alloying (MA) and precipitated during Spark Plasma Sintering (SPS) consolidation. Findings illustrate that co-precipitation effectively produces nano-powders with customised compositions, enriching Y, Ti, and Zr in the ferritic grade to condition subsequent oxide precipitation. While the addition of Y–Ti–Zr–O nano-oxides did not prevent the formation of Y–Al–O and Al-containing nano-oxides, these were refined thanks to the presence of well-dispersed Zr. Additionally, the Spark Plasma Sintering (SPS) parameters were optimised to tailor the bimodal grain size distribution of the ODS steels, aiming for favourable strength-to-ductility ratios. Comprehensive microstructural analyses were performed using SEM, EDS, EBSD, and TEM techniques, alongside mechanical assessments involving microtensile tests conducted at room temperature and small punch tests carried out at room temperature, 300 °C, and 500 °C. The outcomes yielded promising findings, showcasing similar or better performance with conventionally manufactured ODS steels. This reinforces the effectiveness and success of this innovative approach.

1. Introduction

ODS ferritic steels are among the leading candidates for nuclear energy applications, especially for those components exposed to higher operating temperatures. Their good mechanical properties result from the high oxide dispersion into the ferritic matrix, whose pinning effect and high-temperature stability improve the creep behaviour [1–3]. Hence, higher precipitates densities in these steels convey an improved mechanical performance at high working temperatures. Traditionally, the precipitation of these oxides is enabled by adding one oxide precursor (Y_2O_3) and some pure elements such as Ti and Zr in the milling process. In this way, during the subsequent consolidation, a dense population of nanoclusters and nano-oxides precipitate (around 10^{23} oxides/m^3) [4]. The competition established by the different oxides precursors depends directly on their oxygen affinity, quantity, and distribution, producing various oxides with uncertain stoichiometry.

Nonetheless, the problem appears in the Al-containing ODS steels where Al is introduced to optimise the oxidation behaviour by forming Al_2O_3 layers [5–7]. Undoubtedly, part of the this Al reacts with Y_2O_3 forming Y–Al–O oxides during the consolidation step, even in the presence of Ti [8]. These oxides could precipitate as coarse and incoherent oxides, becoming less effective at blocking dislocations and limiting the mechanical response of the steel under high-temperature conditions compared with their analogous without Al [6,8–13]. Usually, these materials' precipitates density (Np) is reduced to 10^{20}-10^{21} oxd/m^3, while the precipitates' mean size could vary from 10 to 30 nm [14–16].

Over the last years, this phenomenon has been solved through different techniques continuously under development and research. On one side, various studies used Zr or Hf (as a pure element or as an oxide) since their affinity with Y and O is more significant than Al, developing

* Corresponding author. Dpt. Materials Science and Engineering, IAAB, Universidad Carlos III de Madrid (UC3M), Av. de la Universidad 30, 28911, Leganés, Spain.
E-mail addresses: juanalberto.meza@uc3m.es (A. Meza), eric.macia@uc3m.es (E. Macía), marta.serrano@ciemat.es (M. Serrano), carmen.merten@ifam-dd.fraunhofer.de (C. Merten), uwe.gaitzsch@ifam-dd.fraunhofer.de (U. Gaitzsch), Thomas.Weissgaerber@ifam-dd.fraunhofer.de (T. Weißgärber), monica.campos@uc3m.es (M. Campos).

https://doi.org/10.1016/j.net.2024.02.018
Received 18 September 2023; Received in revised form 5 February 2024; Accepted 7 February 2024
Available online 9 February 2024
1738-5733/© 2024 Korean Nuclear Society. Published by Elsevier B.V. This is an open access article under the CC BY-NC-ND license (http://creativecommons.org/licenses/by-nc-nd/4.0/).

Y–Zr–O or Y-Hf-O nano-precipitates and leading to an improvement of the mechanical properties maintaining the amount of inserted Al [12,17–23]. This phenomenon is mainly related to the binding energy of Y–Zr–O and Y-Hf-O, which is far superior to Y–Al–O when those compounds are formed in a Fe BCC matrix [19,20,23–27]. On the other side, other authors have been using different nanoparticles developed in an ex-situ way and inserted in the material through mechanical alloying. L. Wang et al. [28,29] demonstrated that inserting $Y_2Ti_2O_7$ nanoparticles reduces the interaction with Al attaining a better response under mechanical requirements.

Following these lines, the innovative aspect proposed in this research is to produce a complex Y–Ti–Zr–O nano-oxide using a co-precipitation method [30]. The idea behind adding the oxide formers elements (Y, Ti, and Zr) as a complex oxide formed by these elements is to generate nanoparticles that would be incorporated into the steels during the mechanical alloying (MA) step. Being nanoparticles, higher dispersion of these elements in the Fe matrix could be expected, resulting in more small environments enriched in Y, Ti and Zr. Thus, during Spark Plasma Sintering (SPS), significant precipitates' densities will be achieved, as studied in Ref. [31], where other ODS steels incorporated the oxides formers following the mentioned strategy. Once the precursor oxide has been synthesised, the development of the ODS steels proceeds by homogeneously mixing these Y–Ti–Zr–O nano-oxides with a prealloyed steel powder (Fe–14Cr–5Al–3W) by using MA and then consolidating the material by SPS.

Furthermore, in previous works, the influence of the selected SPS parameters on the grain microstructure has been studied [22]. These parameters play a strong role by tailoring the formation of ultrafine and micrometric grain regions achieving improved strength/ductility ratios. Thus, the influence of the applied heating rate and sintering temperature are also reported, in an effort to find a competitive ODS steel using this new production method.

Hence, initially to study the effect of the nano-complex oxide addition and the influence of the SPS-parameters, the mechanical behaviour of the processed ODS steels will be tested at room and high temperatures. The alloys will be compared to the SPS-consolidated prealloyed powder and previous 14Al-ODS-Ti[1] without Zr, in order to evaluate the effect of the Zr addition, [32]. Meanwhile, to understand the effect of adding the oxide former elements as a complex nano-oxides, 14AlODS-Zr600 will be used as a reference[2] [22]. Finally, to analyse the materials' behaviour at high temperatures, the results will be compared to those obtained from the ODS steel obtained in the GETMAT project (high-performance ODS steel obtained by hot extrusion) [33,34].

2. Experimental procedure

Gas-atomised prealloyed powders with the ferritic matrix composition, Fe–14Cr–5Al–3W (in wt.%, $d_{50} = 30$ μm, Sandvik Osprey Powder Group) and the co-precipitated complex oxide nanoparticles, Y–Ti–Zr–O (aggregates of $Y_{1.6}Ti_{0.9}Zr_{1.6}O_{7.2}$ nanoparticles around 20 nm in size, composition in atomic fraction measured from EDS point analyses performed in several zones of the compound), which contained the elements responsible of forming the nano-oxides during the consolidation stage were the starting raw materials. This complex oxide was synthesised in-house through a co-precipitation reaction (process described in Ref. [31]), and its amount (0.96 wt%) was calculated to keep the level of Y in 0.20 wt% (analogous to 0.25 wt% of Y_2O_3 addition) [22,23,32].

The MA was performed in a horizontal ZOZ attritor Simoloyer CM01 type under a highly pure Ar atmosphere (99.9995 vol%) after 3 previous vacuum purges to control the quality of the atmosphere. The balls-to-powder ratio was 20:1, and the rotation speed was set up to 800 rpm with an effective milling time of 50 h. XRD characterised milled powders to check it was correctly performed by monitoring the evolution of crystallite size (L) and microstrain values (ε) with milling time (calculations based on applying the Scherrer method in the most intense XRD peak [35]). The interstitial composition (C, O and N) of the powders before and after the MA was determined using LECO TCH 600 and LECO CS230 to control the level of contamination induced in the powders during the MA. A particle size analyser (LA950, Horiba, Japan) with a laser beam was used to measure the particle size distribution. The MA powder morphology was also studied by FEG-SEM (FEI Teneo) and was compared with 14AlODS-Zr milled powders (ODS steel produced through the same route but with the addition of Zr as a pure element) developed in previous studies [22].

SPS was performed in an FCT Systeme GmbH varying the sintering temperatures and heating rates (Table 1). To this end, the ODS powders were introduced into a 20 mm cylindrical graphite die and sintered in vacuum (10^{-2}-10^{-3} mbar). Additionally, a high-purity (>99.97%) tungsten foil (25 μm thick) was used as a diffusion barrier during the SPS process to avoid graphite contamination from the die to the powders [20]. The steels' relative density was studied using image analysis with free software JMicrovision® (after taking several SEM images at different magnifications in each steel, the pores were identified and by taking them as a region percentage, porosity percentages were assessed and transformed in relative densities).

The final microstructure was evaluated by SEM (FEI Teneo), and TEM FEG S/TEM (Talos F200X, FEI, USA) operated at 18 and 200 kV, respectively. For the TEM analysis, the specimens were polished as mirror-like surfaces and then electropolished at −60 °C and 22 mV in a solution of 5% perchloric acid in methanol.

Finally, the material's mechanical properties were evaluated by different techniques. Micro-hardness tests were performed applying a load of 200 g (ZwickRoell microhardness). Tensile tests were conducted using miniature dog bone shape specimens at room temperature [36]. The crosshead displacement was used to calculate the strain and the

Table 1
SPS parameters of processed alloys.

Fixed parameters	Heating rate (°C/min)	Temperature (°C)	Labelled samples
Pressure: 57 MPa, dwell time: 3min	100	1100	**YTiZr100-T1**
		1150	**YTiZr100-T2**
		1200	**YTiZr100-T4**
	300	1150	**YTiZr300-T2**
		1180	**YTiZr300-T3**
		1200	**YTiZr300-T4**
	500	1150	**YTiZr500-T2**

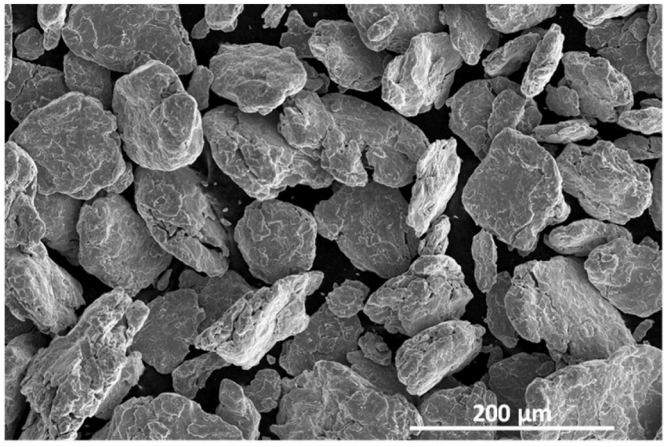


Fig. 1. MA powder after high energy milling of 50 h to introduce the Y–Ti–Zr–O nano-oxides.

[1] Y_2O_3 and pure Ti were added.
[2] Y_2O_3 and pure Ti and Zr were added.

Table 2
Particle size and crystallographic parameters for prealloyed and MA powders.

	d_{10} (μm)	d_{50} (μm)	d_{90} (μm)	L (nm)	ε (%)	ρ_{dis} (m^{-2})	σ_{dis} (MPa)
Preal.14Al powder	12	30	62	43.1	0.217	$1.07{\cdot}10^{15}$	713
MA powder	49	93	182	12	0.758	$1.30{\cdot}10^{16}$	2491

Table 3
Carbon, nitrogen and oxygen analysis of the MA powders (LECO).

	%C	%N	%O	%Ex.O
Preal.14Al powder	0.012	0.007	0.029	–
MA powders	0.094	0.051	0.316	0.06

tensile load was applied with a rate of 2 μm s^{-1}. Small punch tests were performed at a displacement rate of 0.3 mm/min at different temperatures (room temperature, 300 °C, and 500 °C) to evaluate the mechanical response of the steels to this parameter. Discs of 3 mm diameter and 0,250 mm thickness were prepared from the transversal section to the press direction of SPS and were finished as mirror-like surfaces to evaluate the fracture mode and ductility.

3. Results

3.1. Characterisation of the mechanically alloyed powder

After the prealloyed ferritic powder and the synthesised Y–Ti–Zr–O nano-oxides were mechanically alloyed, the powders displayed an irregular morphology and bigger particle size (Fig. 1). After checking in Table 2 the d_{10}, d_{50}, and d_{90} parameters (values used in particle size distribution analysis, representing the particle diameter below which a certain percentage of particles fall) the MA process resulted in a coarsening of the particle size, which was expected since particles deformation-fracture-welding processes occur during the milling process. A bimodal grain size distribution in the SPS-ed steels could provide them with a higher strength-ductility ratio, and to accomplish this, high microstrain levels (ε) and low crystallite sizes (L) must be achieved in the MA powders. Hence, the milling procedure was stopped once the ε and L parameters varied and reached a steady state, as explained in Ref. [22] for similar steels (Table 2).

To study the dislocation hardening effect, the next equation was used as a measure of the degree of plastic deformation achieved during MA. In this case, M was considered as the Taylor factor (3.06) [37], α_d as a constant (1/3) [38], while ρ_{dis} is the dislocation density:

$$\sigma_{dis} = \alpha_d M G b \sqrt{\rho_{dis}} \qquad \text{Eq. 1}$$

To use it, the dislocation density of the milled powders (values shown in Table 2) was calculated using the following equation (b is the Burger's vector, equal to 0.252 nm, assumed for a perfect Fe lattice):

$$\rho_{dis} = 14.4 \frac{\varepsilon^2}{b^2} \qquad \text{Eq. 2}$$

An increase in dislocation density can introduce additional defects into the material, such as stacking faults or sub-grain boundaries, which can act as diffusion pathways or sinks. These defects can enhance diffusion during sintering and so improve the densification during the SPS process. Additionally, they determined the degree of recrystallization that can be achieved following the sintering process.

As an indication of the quality of the powder, after MA process, it is important to measure the level of interstitials in the powder to ensure that it has been properly protected and that contamination has been minimized. In this case, a low level of interstitial elements was achieved and reported in Table 3. The excess of oxygen parameter (Ex.O.) [39] has been determined to check if the oxygen content would be able to promote the formation of the different nano-oxides, while limiting this value to 0.1% as a higher Ex.O. value could reduce the final precipitates' density [40], diminishing the steel's precipitation strengthening.

3.2. Characterisation of the consolidated material

3.2.1. Effect of parameters, heating rate and temperature on the densification of the material

The different parameters used in SPS, such as maximum temperature or heating rate, determined the final microstructure and the attained densification. The effect of the maximum SPS temperature on the density was estimated when the other parameters remained constant, i.e. pressure, holding time and heating rate (HR) (Fig. 2, left). Once a minimum thermal activation was reached, the final density level depended on the heating rate [41]. By increasing it from 100 to 300 °C/min, the densification level increased from 96% to an almost fully dense level, 99%. This effect is clearly seen when a constant SPS temperature was selected (1150 °C) and the HR was changed from 100, 300–500 °C/min (Fig. 2 right).

Regardless of the used SPS conditions, the desired bimodal microstructure was achieved in all the steels just like in previous works [22]. Fig. 3 evinced microstructures with large micrometric grains and ultrafine (UF) grains colonies for the different SPS-ed steels. The addition of the co-precipitated nano-powders (Y–Ti–Zr–O) also influenced on the nano-oxides precipitation (i.e. size, place and composition), and so, the ability of the nano-oxides to retain the grain growth and the stability of the fine microstructure.

Fig. 3 also showed, on one side, the effect of the HR (300–500 °C/min) when maintaining the same sintering temperature of 1150 °C (YTiZr300-T_2 and YTiZr500-T_2). Analogously, the effect of the sintering temperature was determined on the samples by keeping constant the HR (YTiZr300-T_3 and YTiZr300-T_4) [42,43].

In relation to the heating rate and sintering temperature, it should be noted that in these steels, a HR of 300 °C/min had no effect on the

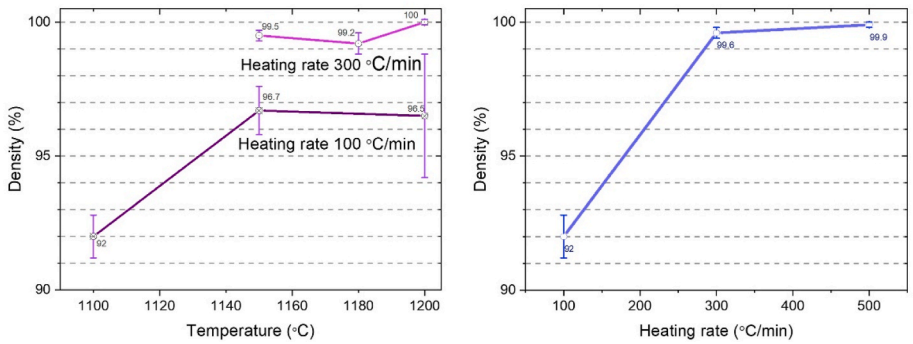


Fig. 2. (Left) Density vs temperature and heating rate. (Right) Density vs heating rate when SPS is performed at 1150 °C.

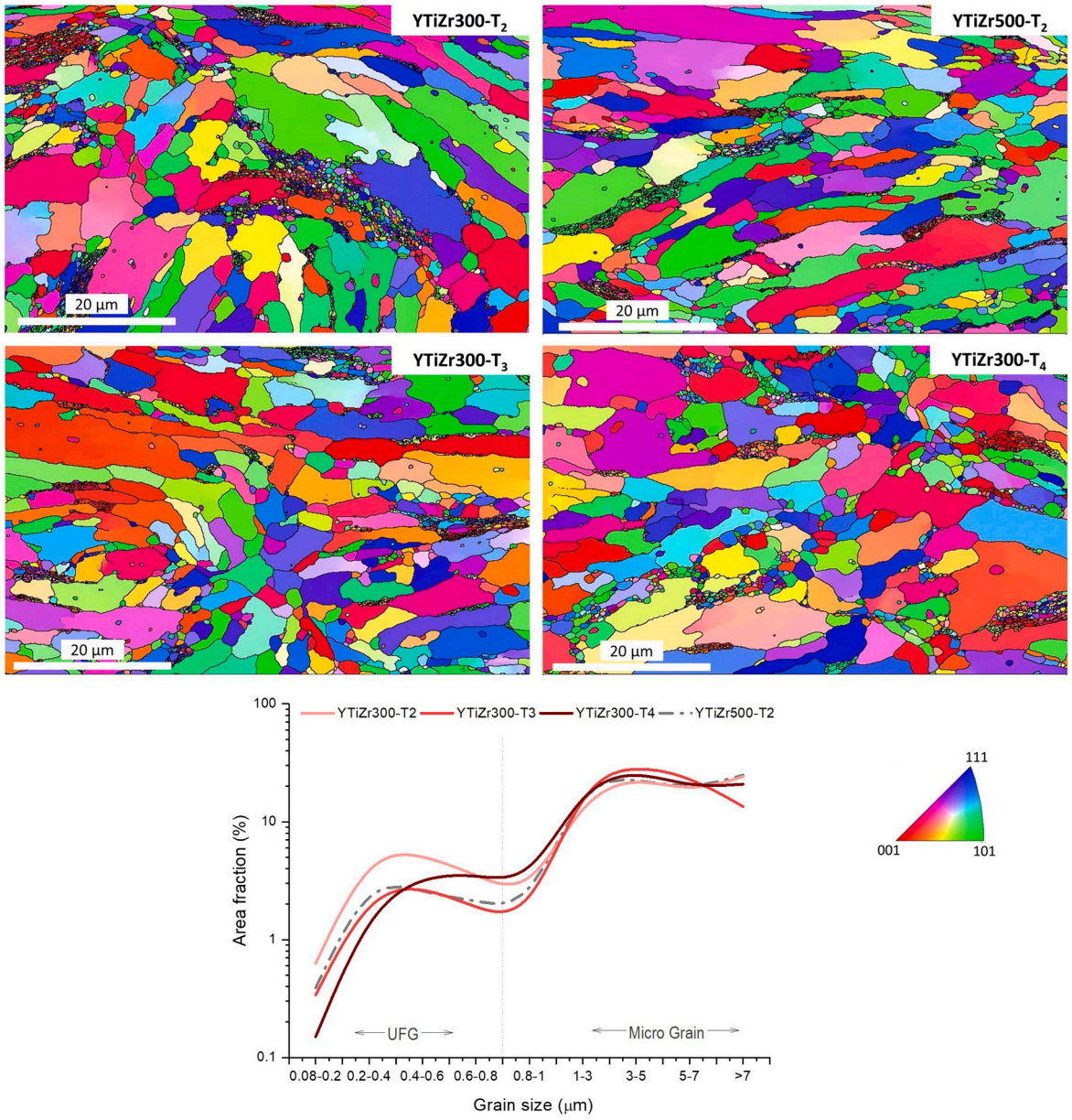


Fig. 3. Inverse pole Figure maps (Y direction) and grain area fraction distribution on the SPS-ed ODS steels.

Table 4
UF area fractions, average grain size of micrometric and UF grains, and dislocation densities of the ODS steels.

	YTiZr500-T_2	YTiZr300-T_2	YTiZr300-T_3	YTiZr300-T_4	14AlODS-Zr600 [22]
UF area fraction (%)	4.3 ± 2.3	14.4 ± 5.1	6.1 ± 1.9	1.8 ± 0.5	32 ± 13
UF grain size (μm)	0.31	0.31	0.32	0.40	0.30
Micrograin size (μm)	2.36	2.17	2.40	2.10	1.51
$\rho_{dislocation}$ (m^{-2})		$5.09{\cdot}10^{14}$	$4.40{\cdot}10^{14}$	$3.82{\cdot}10^{14}$	$9.07{\cdot}10^{14}$

regions of UF grains. Furthermore, specimens processed up to 1180 °C (T_3) at 300 °C/min suffered a decrease in the amount of UF grain colonies. As expected, no texture was observed on the consolidated samples.

In terms of microstructure, these steels are comparable to the ones previously processed in Ref. [22] (see Table 4). In both UF and micrometric zones, the average grain size is analogous, and the final dislocation density is determined by the temperature of the process when the heating rate is kept constant. However, a clear drop in the ultrafine regions (UF area fraction%) can be observed when compared with the 14AlODS-Zr600 steel from Ref. [22] although this steel does not follow the same processing route nor does it have the same composition. In this last steel the added wt. % of Zr is considerably higher than in the steels developed in this work, which in return, promotes a higher denisity of precipitates in charge of blocking the grain boundaries and so, promoting the formation of more UF regions that strengthen the steel by grain size strengthening.

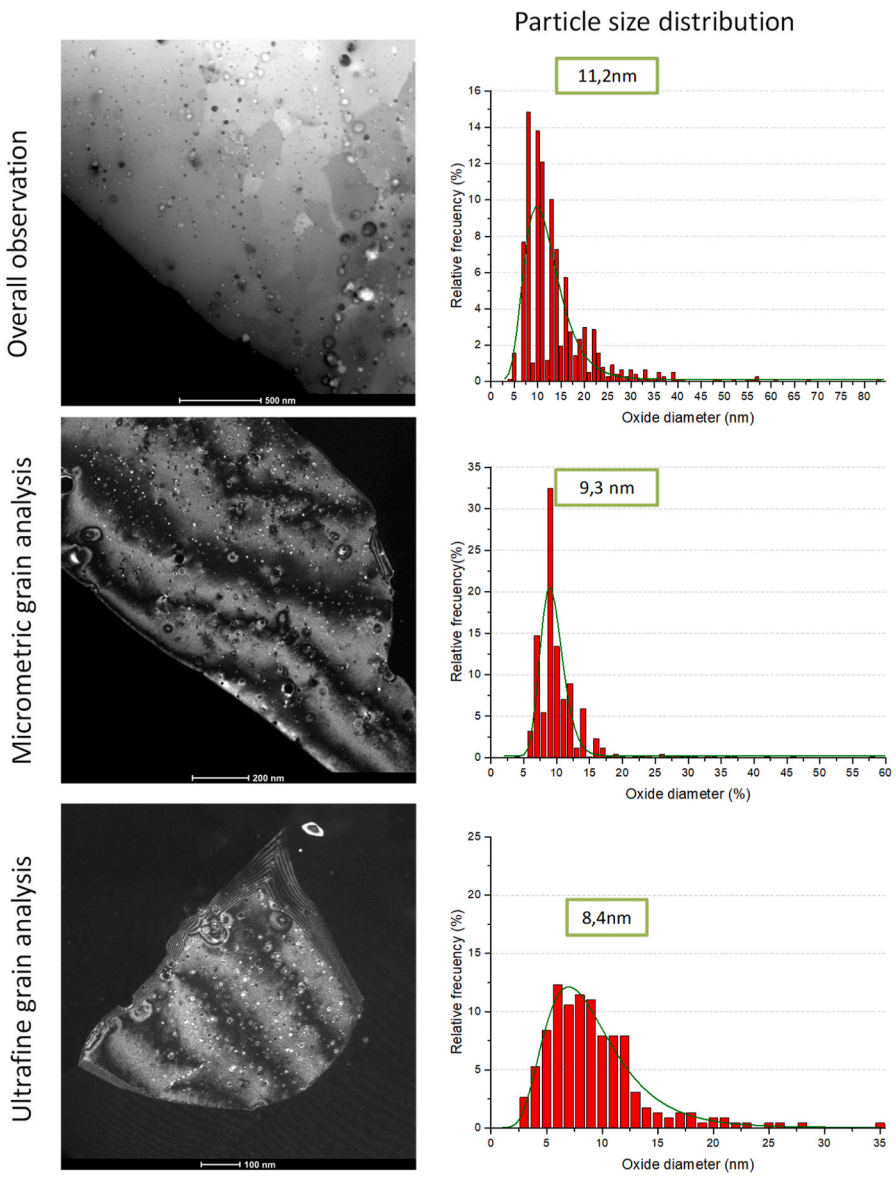


Fig. 4. STEM characterisation on YTiZr500-T_2: (left) STEM Images, (right) oxide diameter distribution.

Because all the contrasted steels were fabricated through the same powder metallurgy route (MA + SPS), their grain microstructures have comparable grain morphologies, and none exhibit any principal crystallographic directions (no texture). Thus, the effect of the matrix texture has not been considered for this study.

3.2.2. *Characterisation of the nano-precipitates*

The characterisation of the composition, size, morphology, and distribution of the oxides is shown in Fig. 4. The precipitates density ($N_p \approx 10^{21}$ oxd/m^3) was in the same order of magnitude as other ODS steels processed by SPS without Zr [8,44] and similar ranges of other ferritic ODS steels with Zr developed by Gao et al. [18]. A total amount of 2000 nano-oxides were measured to obtain the final size distributions, where the average oxide diameter varied from 8.4 to 11.2 nm.

The distribution of nano-oxides with respect to grain size has been investigated separately in the micrometric and ultrafine zones (Fig. 4). Considering the micrometric grains, a total area of $2{\cdot}10^6$ nm^2 containing 693 oxides was analysed. The precipitates size distribution is centred at 9.3 nm, and the total density of precipitates measured is $3.45{\cdot}10^{21}$ oxd/m^3 which provided a volumetric fraction of 0.14%.

(wt %)	Fe	Cr	W	Al	Y	Ti	Zr	O
Y-Zr-Ti-Al-O, Type 1	53.64	6.49	0.68	**12.81**	**4.82**	**2.74**	**2.25**	**16.57**
Y-Zr-Al-O, Type 2	22.36	7.31	1.11	**29.24**	**4.34**	0	**4.12**	**31.52**
Y-Al-O, Type 3	37.83	11.89	1.3	**15.04**	**5.43**	0	0	**28.51**
Y-Zr-O, Type 4	57.44	11.77	6.71	**2.79**	**5.01**	**0**	**5.98**	**10.29**

Fig. 5. Oxides detected on YTiZr500-T_2: Average composition (wt.%) of the different precipitates by EDX on TEM.

Ultrafine regions were also investigated to observe if the composition or the density of oxides had changed in these smaller grains. A total area of $3.2{\cdot}10^5$ nm^2 was analysed in which the oxide size distribution was centred at 8.4 nm. Moreover, in these regions the density of precipitates increased to $7.14{\cdot}10^{21}$ oxd/m^3 (frequency of 0.22 %) which can explain the lower local grain growth in contrast to the micrometric area. Certainly, EDX by TEM exposed oxides containing the elements that

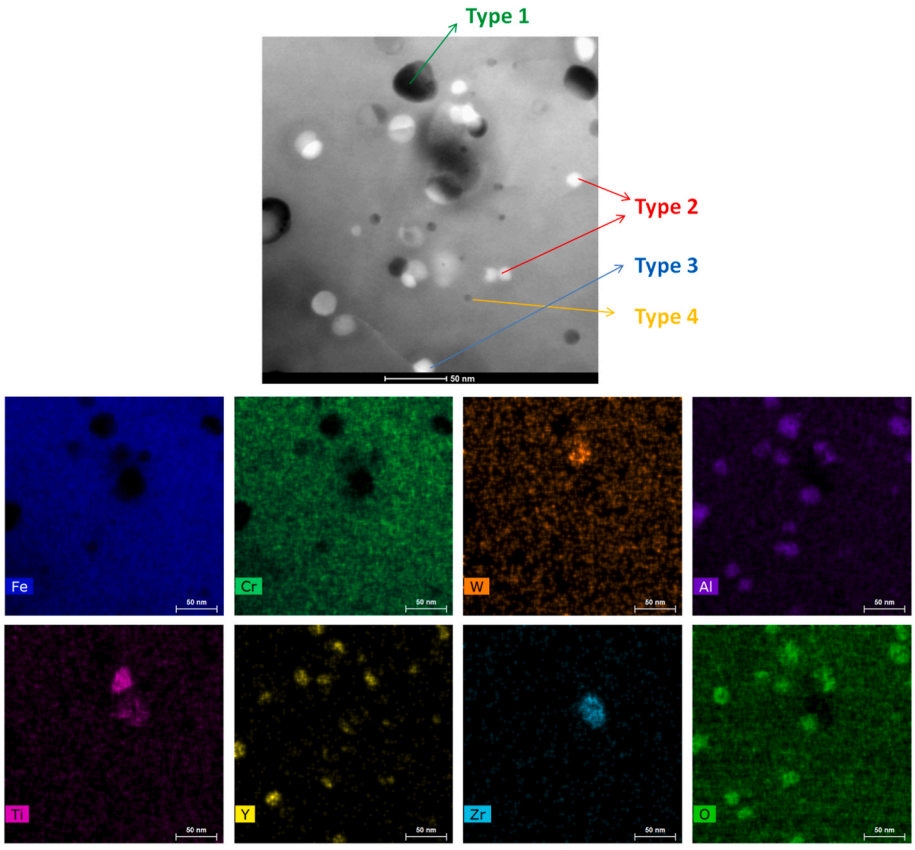


Fig. 6. EDS Mapping of YTiZr500-T_2.

Table 5
Total number of analysed nano-precipitates and their fractions of Y, Zr, Ti and Al.

(total n of precipitates)	Y	Zr	Ti	Al
108	99 (91.6%)	86 (79.6%)	62 (57.40%)	78 (72.22%)

were previously precipitated in the complex oxide, Y–Ti–Zr–O. Four types of precipitates were detected (summed up on Fig. 5), namely:

Type 1 (Y–Ti–Zr–Al–O): These precipitates were the most common in the steels and were located both inside the grains and in the grain boundaries, exhibiting sizes from 10 to 30 nm (displaying a white contrast) even when only a few of them ranged between 30 and 90 nm. From 30 to 90 nm, precipitates presented a black colour contrast even if the composition had not changed.

Type 2 (Y–Zr–Al–O): With sizes between 9 and 30 nm and a white contrast, they were located inside the grains.

Type 3 (Y–Al–O): Their sizes were in the range of 15–45 nm and were situated inside the grains and at the grain boundaries.

Type 4 (Y–Zr–O): Sizes ranging from 8 to 20 nm, mainly located inside the grains.

These oxides were clearly appreciated on Fig. 6, where the compositional mappings were in accordance with the previous classification.

Although elements with higher oxygen affinity were introduced to

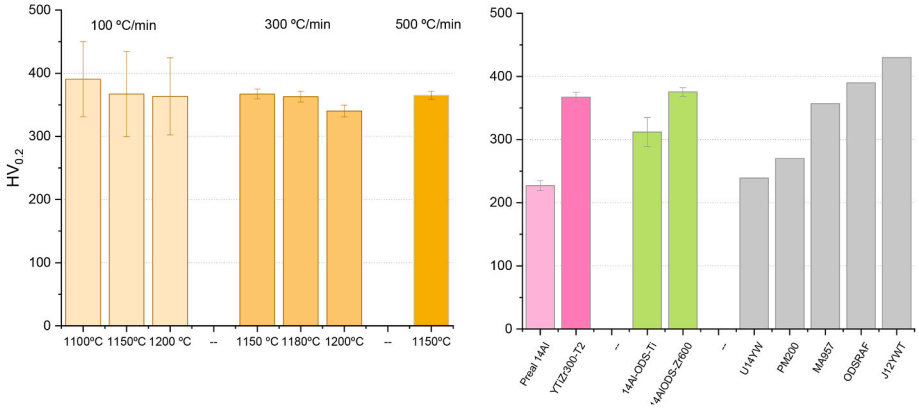
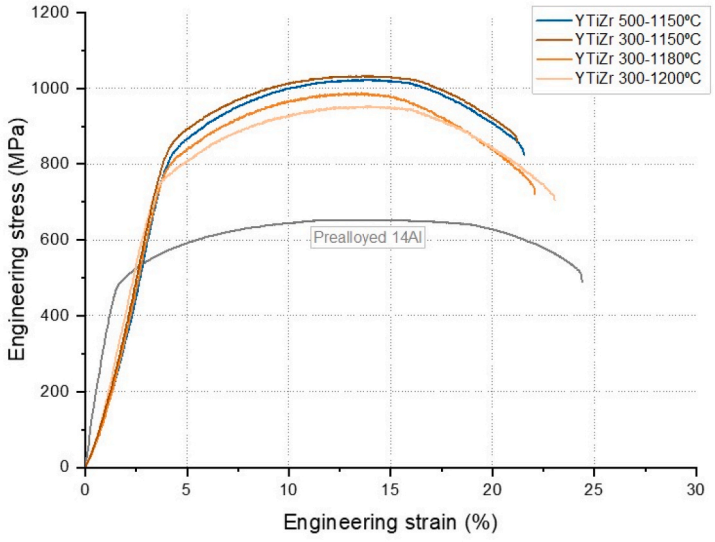


Fig. 7. Microhardness evaluation depending on different SPS parameters and comparison with Zr600 from Ref. [22], free Zr ODS (14Al-ODS-Ti), free ODS ferritic steel (Prealloyed 14Al) and ODS steels from the literature.



	UTS (MPa)	YS (MPa)	Toughness (MPa)	Total Deformation (%)	
YTiZr500-T_2	1001 ± 21	815 ± 18	177 ± 12	21.51 ± 1.38	H.R. Effect
YTiZr300-T_2	1021 ± 23	841 ± 16	174 ± 29	21.04 ± 3.86	
YTiZr300-T_3	969 ± 20	793 ± 20	183 ± 5	22.73 ± 0.48	T Effect
YTiZr300-T_4	935 ± 14	735 ± 25	190 ± 11	24.23 ± 1.79	

Fig. 8. Comparison of engineering tensile stress-strain curves for the steels, ODS Zr free (14Al-ODS-Ti) and free ODS ferritic steel (Prealloyed 14Al).

minimise the Y–Al–O oxides formation, the higher Al content of the base prealloyed powder promoted the presence of these. Still, the formation of complex oxides such as Y–Ti–Zr–Al–O (type 1 oxides), with more refined diameters than Y–Al–O, was observed, representing the highest volume of the precipitated oxides. Moreover, from the whole analysed oxides, 80% has Zr, as it is shown in Table 5. This is due to the addition of the Y–Ti–Zr–O compound, which increased the formation of type 1 nano-oxides.

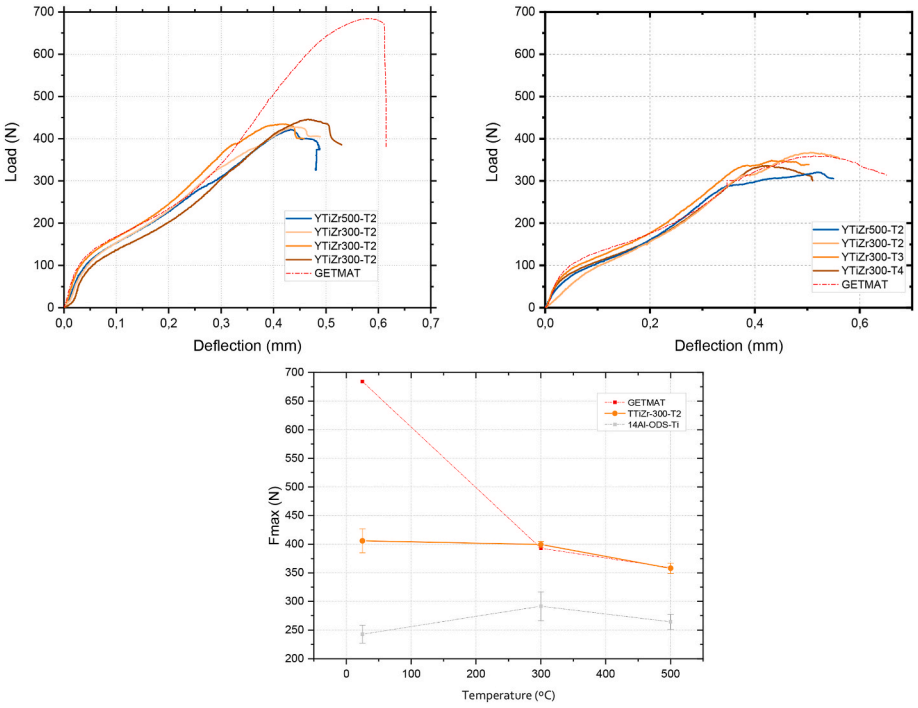


Fig. 9. Small punch test at RT and 500 °C and maximum load values achieved at different temperatures. Graphs show the comparison between F-ODS-II alloys, Zr600 (14ZrODS) and GETMAT steel (processed by HE [33,34]).

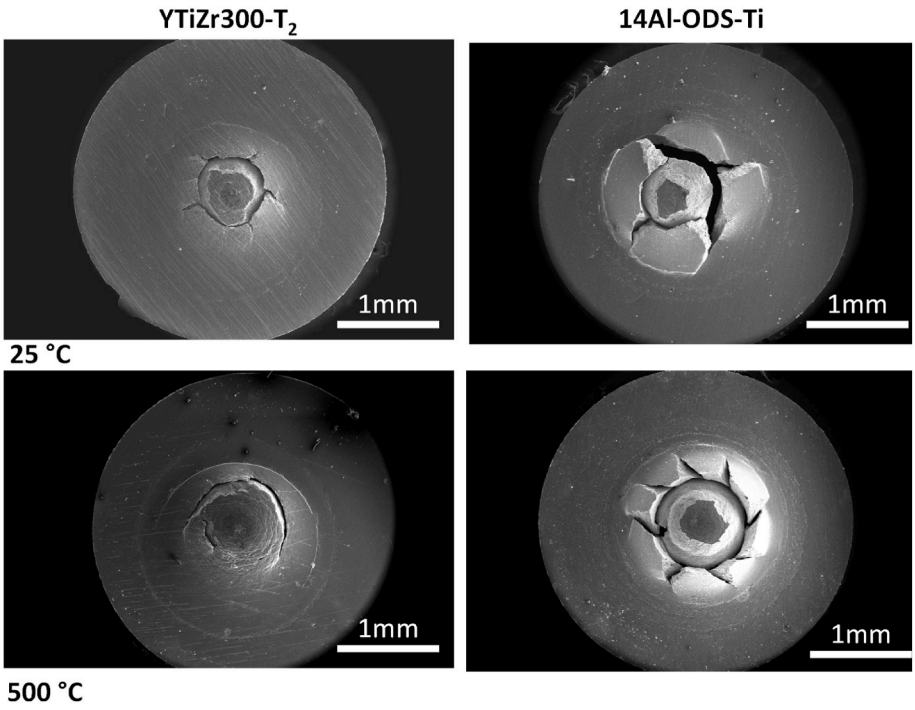


Fig. 10. Small Punch fracture specimens.

3.3. Mechanical response on F-ODS-II materials

3.3.1. Room temperature behaviour

The capability of the material to withstand plastic deformation was evaluated by microhardness testing (Fig. 7).

Because of the lower densification of the samples consolidated at 100 °C/min (relative density of 96%) the microhardness values have the highest deviations, but the values remain comparable to those obtained at higher HR (300 and 500 °C/min). As a result of improving the density by increasing the HR, the values became more stable and repeatable.

Regarding their comparison with other ODS steels from the literature, it should be noted that YTiZr300-T_2 has achieved a comparable value to 14Al-ODS-Zr600, even if this last one showed higher precipitates density values and lower regions of UF grains. Therefore, the SPS-ed steels from this work produced an oxide more effective at blocking dislocations than the one produced in 14AlODS-Zr600 [23]. Besides, as expected, these steels with more refined oxides improved their hardness with respect to the one developed without Zr [32], and the other steels reported in Refs. [45,46].

A microtensile test was also performed on alloys with densities greater than 98% (Fig. 8). Despite the SPS conditions, all materials showed outstanding UTS values as well as proper toughness levels. The YTiZr300-T2 alloy had the best balance of tensile properties, corresponding to one with a significantly high precipitates density value and the highest percentage of ultra-fine grain colonies.

The effect of HR is negligible in this case, since both alloys (YTiZr500-T2, YTiZr300-T2) reached similar temperatures. As HR increased, the differences in density did not represent a notable improvement in tensile strength, and the YTiZr500-T2 alloy has less ultrafine grain colonies, which are probably responsible for its lower strength.

In view of the bimodal grain size, the processed ferritic ODS steels could be considered heterogeneous materials with notable differences in ductility or strength between the micrometric and UF grain colonies. Thus, during the microtensile tests, both areas behaved differently. Once the ductile area overcame the elastic deformation, the harder one (ultrafine colonies) remained elastic, limiting the further, plastic deformation of the ductile areas. Therefore, an increase in the macroscopic YS of the material was measured. On the other hand, for higher stress levels, the softer micrometric grains sustained much harder strain, and therefore the material's toughness was improved. The formed nano-oxides effectively blocked the dislocation movement, which resulted in an enhanced UTS.

The amount of UF grain colonies decreased when SPS was performed at 1200 °C and 300 °C/min (YTiZr300-T_4), which explained the reduction in the UTS. Once again, the ODS steels developed in this investigation have achieved properties comparable to 14AlODS-Zr600 [22].

3.3.2. High-temperature evaluation

The results obtained by Small Punch tests are represented through the load-deflection curves (Fig. 9). The microstructures promoted by the nano-complex oxides and the dual grain size achieved make the difference with respect to the benchmark 14Al-ODS-Ti [31] composition (ODS steel without Zr) tested in the same conditions. However, as it was observed in tensile tests at room temperature, no difference was noticed between the reference alloy 14AlODS-Zr600 [22] and the processed Y–Ti-ZrX00 alloys from this work. Regardless of how Zr was included in the composition, this element seems to be the key factor in the improvement of mechanical properties. Proposed alloys can be compared to GETMAT in terms of maximum load at high temperatures (300 and 500 °C). At 300 °C, the developed alloy maintains the maximum load obtained at room temperature and only drops slightly at 500 °C.

The overall appearance of the fractured surfaces was observed to provide insights into the fracture mode (Fig. 10). The proposed alloys present ductile-brittle fracture mode with cracks open and circumferentially oriented (like 14AlODS-Zr600). The energy absorption capability found in the Zr-free ODS alloys (14Al-ODS-Ti) was improved, as in these last ones the fracture mode was brittle with radial cracks.

4. Discussion

4.1. Influence of complex oxide addition on the composition of nano-precipitates

The composition of precipitates in free Al ferritic ODS steels has been

Table 6
Yield strength values for the processed ODS steels calculated theoretically vs. experimentally obtained YS (in MPa).

		YTiZr500-T_2	YTiZr300-T_2	YTiZr300-T_3	YTiZr300-T_4
Strengthening contribution	σ_{gb}	189	226	193	191
	σ_{disl}	493	492	458	427
	σ_p	122	122	122	122
Calculated YS	$\sigma_{y,calc}$	891	927	861	829
Experimental YS	$\sigma_{y,experimental}$	815	841	793	735

studied in other works and demonstrated that additions of Zr, Ti and Y_2O_3 formed Y–Ti–Zr–O type nano-precipitates. The presence of this type of precipitates favours their stability on the attained microstructure [47,48].

The reaction of the solute elements with oxygen leads to the production of precipitates with specific compositions. When Y, Ti and Zr are in a free state, and not in the ferritic matrix, their interaction with oxygen is guaranteed and their binding energy with O follows the next trend Zr–O > Y–O > Al–O. However, Y, Zr, and Al are highly influenced by the environment/structure in which they are inserted (in this case, the BCC Fe structure), and their behaviour changes along the following trend Y–O > Zr–O > Al–O. This phenomenon is explained in Ref. [49] through the formation energy of the solute element in the Fe matrix since there is a relationship between the formation of the different precipitates with the binding energy between the oxide formers, the vacancies, the surrounding BCC matrix and the oxygen. Under these conditions, the precipitation trend would be Fe–Y > Fe–Zr > Fe–Al, i.e., Y and Zr are more likely to precipitate than Al.

The high concentration of vacancies promoted during MA, also determines the formation of nanoclusters (or nano-oxides), as reported in Refs. [50–54]. These investigations show the relationship established between the different solutes with the vacancies considering the binding energy and their affinity, reaching the conclusion that the binding energy when a solute atom interacts with a vacancy follows the trend Y-□ > Zr-□ > Al-□.[3] If the presence of oxygen is included, they show that the maximum binding energy for Zr–O-□ is higher than Al–O-□ [47]. This explains why Y–Zr–O, Y–Al–O, Y–Zr–Al–O, or Y–Zr–Ti–O represent almost the totality of the nano-precipitates formed in the ODS steels of this work whereas Zr–O, Y–O, Ti–O, Al–O, ZrY, or TiY were not identified.

It was impossible to avoid forming type 3 Y–Al–O oxides due to the high Al content in the composition (5%). Besides, in the BCC matrix, Al has a diffusion rate similar to Fe. As a result, the formation of Y–Al–O is facilitated by a shorter diffusion distance to react with O, like what has been reported by Unocic et al. in Ref. [24]. Thus, Al would be more likely to react than the other elements.

4.2. Heating rate effect on the final consolidation of material

A parameter studied to improve the density of SPS samples is the heating rate. According to two main theories over the last few years, this improvement in densification can be explained by two factors [41–43,55]. Some authors argue that changing this parameter can affect the Joule effect, since the intensity of the current affects the temperature gradient [56]. The surface of the particles has a higher activation to form sintering necks since higher temperatures are reached [57,58]. At the same time, the high density of lattice defects limits the thermal conductivity and so, creates a shell/core distribution of temperatures, with a gradient from the surface to the centre of the particles. Thus, porosity between particles is reduced more effectively while limiting excessive grain growth inside the particles. Other works have indicated that the main responsible of enhanced densification is an overheating of the entire mass of powder (up to 100 °C) as the intensity of the current is increased when the H.R. is increased [59,60].

4.3. Mechanical behaviour: room temperature conditions

The Zr addition is crucial to attain proper mechanical properties since improvements are observed with respect to free Zr ODS ferritic steel (14Al-ODS-Ti). To explain why, it is possible to analyse the yield strength (σ_y) of ODS steels, which depends on different mechanisms as reported in Ref. [61].

$$\sigma_y = \sigma_0 + \sigma_{ss} + \sigma_{gb} + \sqrt{\sigma_{dis}{}^2 + \sigma_p{}^2} \quad \text{(eq 3)}$$

In this equation σ_0 and σ_{ss} are constants representing the friction stress of a single pure Fe crystal (53.9 MPa as reported in Ref. [62]) and the strengthening by solid-solution strengthening (following the work of [22], 140 MPa) respectively. Grain boundary strengthening, dislocation and dispersion strengthening are dependent on the processing route and composition and can therefore vary with the developed microstructure. Using the same formulas as in Ref. [22] allowed to obtain the results from Table 6.

The dislocation density strengthening and oxide strengthening provided the largest contribution to the calculation of σ_y [63–65]. Increments in the sintering temperature involved a decrease in grain boundary strengthening, which could explain the variation in the calculated σ_y of ODS steels. Even though the experimental and theoretical values differ, the relative magnitude of the σ_y is maintained between manufactured ODS steels.

Clearly, the increment order of non-constant strengthening contributions is $\sigma_{dis} > \sigma_{gb} > \sigma_p$. Therefore, yield strength is primarily influenced by dislocation and grain boundary strengthening, which account for about 75% of the strength.

5. Conclusions

A new method to accomplish the addition of oxide formers in the production of a ferritic ODS has been developed. Thanks to the co-precipitation technique it is possible to design and tailor complex nano-oxides that can be introduced during MA, and later precipitated during the SPS consolidation. It was demonstrated that:

- Co-precipitation could be an effective method to obtain nano-powders with a tailored composition. Enriched environments of Y, Ti and Zr were produced on the ferritic grade by adding a unique compound of oxide formers, which in the end conditioned the later oxide precipitation.
- The addition of Y–Ti–Zr–O nano-oxides did not avoid the formation of Y–Al–O (type 4) or Al-containing nano-oxides (Type 1 and type 2).
- SPS conditions can be optimised to obtain a fully dense material. The heating rate was the key factor that enabled full densification of the steels when the applied pressure was 50 MPa.
- A bimodal grain size distribution was obtained for all the consolidated samples. The oxides produced, were effective in retaining grain growth. The sizes of the ultrafine colonies depended on the maximum temperature achieved on SPS.
- The evaluated mechanical properties have shown the proper behaviour of the produced ODS steels by this new method. Small

[3] The □ symbol represents a vacancy.

punch tests at high T showed promising results at 300 °C and 500 °C where the steels achieved optimum values, similar to the ones obtained by traditional methods of production.

Declaration of competing interest

The authors declare that they have no known competing financial interests or personal relationships that could have appeared to influence the work reported in this paper.

Acknowledgments

The research leading to these results has received funding from Spanish Ministry of Science, Innovation and Universities under project MAT2013-47460-C5-5-P and MAT2016-80875-C3-3-R. Daniel Plaza López is sincerely thanked for his help with the Small Punch tests.

References

[1] S.J. Zinkle, J.L. Boutard, D.T. Hoelzer, A. Kimura, R. Lindau, G.R. Odette, M. Rieth, L. Tan, H. Tanigawa, Development of next generation tempered and ODS reduced activation ferritic/martensitic steels for fusion energy applications, Nucl. Fusion 57 (2017) 17, https://doi.org/10.1088/1741-4326/57/9/092005.

[2] N. Cunningham, Y. Wu, D. Klingensmith, G.R. Odette, On the remarkable thermal stability of nanostructured ferritic alloys, Mater. Sci. Eng. A. 613 (2014) 296–305, https://doi.org/10.1016/j.msea.2014.06.097.

[3] M.K. Miller, D.T. Hoelzer, E.a. Kenik, K.F. Russell, Stability of ferritic MA/ODS alloys at high temperatures, Intermetallics 13 (2005) 387–392, https://doi.org/10.1016/j.intermet.2004.07.036.

[4] S. Ukai, M. Fujiwara, Perspective of ODS alloys application in nuclear environments, J. Nucl. Mater. 307–311 (2002) 749–757, https://doi.org/10.1016/S0022-3115(02)01043-7.

[5] S. Takaya, T. Furukawa, G. Müller, A. Heinzel, A. Jianu, A. Weisenburger, K. Aoto, M. Inoue, T. Okuda, F. Abe, S. Ohnuki, T. Fujisawa, A. Kimura, Al-containing ODS steels with improved corrosion resistance to liquid lead–bismuth, J. Nucl. Mater. 428 (2012) 125–130, https://doi.org/10.1016/j.jnucmat.2011.06.046.

[6] T. Liu, C. Wang, H. Shen, W. Chou, N.Y. Iwata, A. Kimura, The effects of Cr and Al concentrations on the oxidation behavior of oxide dispersion strengthened ferritic alloys, Corrosion Sci. 76 (2013) 310–316, https://doi.org/10.1016/j.corsci.2013.07.004.

[7] S. Ohtsuka, T. Kaito, M. Inoue, T. Asayama, S.W. Kim, S. Ukai, T. Narita, H. Sakasegawa, Effects of aluminum on high-temperature strength of 9Cr-ODS steel, J. Nucl. Mater. (2009) 386–388, https://doi.org/10.1016/j.jnucmat.2008.12.147, 479–482.

[8] C.H. Zhang, A. Kimura, R. Kasada, J. Jang, H. Kishimoto, Y.T. Yang, Characterization of the oxide particles in Al-added high-Cr ODS ferritic steels, J. Nucl. Mater. 417 (2011) 221–224, https://doi.org/10.1016/j.jnucmat.2010.12.063.

[9] R. Kamikawa, S. Ukai, S. Kasai, N. Oono, S. Zhang, Y. Sugino, H. Masuda, E. Sato, Cooperative grain boundary sliding in creep deformation of FeCrAl-ODS steels at high temperature and low strain rate, J. Nucl. Mater. 511 (2018) 591–597, https://doi.org/10.1016/j.jnucmat.2018.04.050.

[10] M.K. Miller, C.M. Parish, Role of alloying elements in nanostructured ferritic steels, Mater. Sci. Technol. 27 (2011) 729–734, https://doi.org/10.1179/1743284710Y.0000000039.

[11] P. Dou, A. Kimura, T. Okuda, M. Inoue, S. Ukai, S. Ohnuki, T. Fujisawa, F. Abe, Effects of extrusion temperature on the nano-mesoscopic structure and mechanical properties of an Al-alloyed high-Cr ODS ferritic steel, J. Nucl. Mater. 417 (2011) 166–170, https://doi.org/10.1016/j.jnucmat.2011.01.061.

[12] A. Kimura, R. Kasada, N. Iwata, H. Kishimoto, C.H. Zhang, J. Isselin, P. Dou, J. H. Lee, N. Muthukumar, T. Okuda, M. Inoue, S. Ukai, S. Ohnuki, T. Fujisawa, T. F. Abe, Development of Al added high-Cr ODS steels for fuel cladding of next generation nuclear systems, J. Nucl. Mater. 417 (2011) 176–179, https://doi.org/10.1016/J.JNUCMAT.2010.12.300.

[13] H.S. Cho, A. Kimura, S. Ukai, M. Fujiwara, Corrosion properties of oxide dispersion strengthened steels in super-critical water environment, J. Nucl. Mater. 329–333 (2004) 387–391, https://doi.org/10.1016/j.jnucmat.2004.04.040.

[14] K. Dawson, S.J. Haigh, G.J. Tatlock, A.R. Jones, Nano-particle precipitation in mechanically alloyed and annealed precursor powders of legacy PM2000 ODS alloy, J. Nucl. Mater. 464 (2015) 200–209, https://doi.org/10.1016/j.jnucmat.2015.04.039.

[15] A. Wasilkowska, M. Bartsch, U. Messerschmidt, R. Herzog, A. Czyrska-Filemonowicz, Creep mechanisms of ferritic oxide dispersion strengthened alloys, J. Mater. Process. Technol. 133 (2003) 218–224, https://doi.org/10.1016/S0924-0136(02)00237-6.

[16] J.H. Schneibel, M. Heilmaier, W. Blum, G. Hasemann, T. Shanmugasundaram, Temperature dependence of the strength of fine- and ultrafine-grained materials, Acta Mater. 59 (2011) 1300–1308, https://doi.org/10.1016/j.actamat.2010.10.062.

[17] P. Dou, A. Kimura, R. Kasada, T. Okuda, M. Inoue, S. Ukai, S. Ohnuki, T. Fujisawa, F. Abe, TEM and HRTEM study of oxide particles in an Al-alloyed high-Cr oxide dispersion strengthened steel with Zr addition, J. Nucl. Mater. 444 (2014) 441–453, https://doi.org/10.1016/j.jnucmat.2013.10.028.

[18] R. Gao, T. Zhang, X.P. Wang, Q.F. Fang, C.S. Liu, Effect of zirconium addition on the microstructure and mechanical properties of ODS ferritic steels containing aluminum, J. Nucl. Mater. 444 (2014) 462–468, https://doi.org/10.1016/j.jnucmat.2013.10.038.

[19] J. Isselin, R. Kasada, A. Kimura, T. Okuda, M. Inoue, S. Ukai, S. Ohnuki, T. Fujisawa, F. Abe, Effects of Zr addition on the microstructure of 14%Cr4%Al ODS ferritic steels, Mater. Trans. 51 (2010) 1011–1015, https://doi.org/10.2320/matertrans.MBW200923.

[20] A. García-Junceda, N. García-Rodríguez, M. Campos, M. Cartón-Cordero, J. M. Torralba, Effect of zirconium on the microstructure and mechanical properties of an Al-alloyed ODS steel consolidated by FAHP, J. Am. Ceram. Soc. 98 (2015) 3582–3587, https://doi.org/10.1111/jace.13691.

[21] K.A. Unocic, B.A. Pint, D.T. Hoelzer, Advanced TEM characterization of oxide nanoparticles in ODS Fe–12Cr–5Al alloys, J. Mater. Sci. 51 (2016) 9190–9206, https://doi.org/10.1007/s10853-016-0111-5.

[22] E. Macía, A. García-Junceda, M. Serrano, M. Hernández-Mayoral, L.A. Diaz, M. Campos, Effect of the heating rate on the microstructure of a ferritic ODS steel with four oxide formers (Y-Ti-Al-Zr) consolidated by spark plasma sintering (SPS), J. Nucl. Mater. 518 (2019) 190–201, https://doi.org/10.1016/j.jnucmat.2019.02.043.

[23] A. García-Junceda, E. Macía, D. Garbiec, M. Serrano, J.M. Torralba, M. Campos, Effect of small variations in Zr content on the microstructure and properties of ferritic ODS steels consolidated by SPS, Metals 10 (2020) 348, https://doi.org/10.3390/met10030348.

[24] H. Xu, Z. Lu, D. Wanga, C. Liu, Effect of zirconium addition on the microstructure and mechanical properties of 15Cr-ODS ferritic Steels consolidated by hot isostatic pressing, Fusion Eng. Des. 114 (2017) 33–39, https://doi.org/10.1016/J.FUSENGDES.2016.11.011.

[25] H. Dong, L. Yu, Y. Liu, C. Liu, H. Li, J. Wu, Enhancement of tensile properties due to microstructure optimization in ODS steels by zirconium addition, Fusion Eng. Des. 125 (2017) 402–406, https://doi.org/10.1016/J.FUSENGDES.2017.03.170.

[26] W. Li, T. Hao, R. Gao, X. Wang, T. Zhang, Q. Fang, C. Liu, The effect of Zr, Ti addition on the particle size and microstructure evolution of yttria nanoparticle in ODS steel, Powder Technol. 319 (2017) 172–182, https://doi.org/10.1016/J.POWTEC.2017.06.041.

[27] L. Zhang, L. Yu, Y. Liu, C. Liu, H. Li, J. Wu, Influence of Zr addition on the microstructures and mechanical properties of 14Cr ODS steels, Mater. Sci. Eng. A. 695 (2017) 66–73, https://doi.org/10.1016/J.MSEA.2017.04.020.

[28] T. Liu, L. Wang, C. Wang, H. Shen, H. Zhang, Feasibility of using Y2Ti2O7 nanoparticles to fabricate high strength oxide dispersion strengthened Fe-Cr-Al steels, Mater. Des. 88 (2015) 862–870, https://doi.org/10.1016/j.matdes.2015.08.118.

[29] L. Wang, Z. Bai, H. Shen, C. Wang, T. Liu, Creation of Y2Ti2O7 nanoprecipitates to strengthen the Fe-14Cr-3Al-2W steels by adding Ti hydride and Y2O3 nanoparticles, J. Nucl. Mater. 488 (2017) 319–327, https://doi.org/10.1016/j.jnucmat.2017.03.015.

[30] T.A. Schaedler, W. Francillon, A.S. Gandhi, C.P. Grey, S. Sampath, C.G. Levi, Phase evolution in the YO1.5-TiO2-ZrO2 system around the pyrochlore region, Acta Mater. 53 (2005) 2957–2968, https://doi.org/10.1016/j.actamat.2005.03.010.

[31] A. Meza, E. Macía, A. García-Junceda, L.A. Díaz, P. Chekhonin, E. Altstadt, M. Serrano, M.E. Rabanal, M. Campos, Development of new 14 Cr ODS steels by using new oxides formers and B as an inhibitor of the grain growth, Metals 10 (2020) 1–16, https://doi.org/10.3390/met10101344.

[32] N. García-Rodríguez, M. Campos, J.M. Torralba, M.H. Berger, Y. Bienvenu, Capability of mechanical alloying and SPS technique to develop nanostructured high Cr, Al alloyed ODS steels, Mater. Sci. Technol. 30 (2014) 1676–1684, https://doi.org/10.1179/1743284714Y.0000000595.

[33] M. Serrano, M. Hernández-Mayoral, A. García-Junceda, Microstructural anisotropy effect on the mechanical properties of a 14Cr ODS steel, J. Nucl. Mater. 428 (2012) 103–109, https://doi.org/10.1016/J.JNUCMAT.2011.08.016.

[34] M. Serrano, A. García-Junceda, R. Hernández, M.H. Mayoral, On anisotropy of ferritic ODS alloys, Mater. Sci. Technol. 30 (2014) 1664–1668, https://doi.org/10.1179/1743284714Y.0000000552.

[35] J.R. Fermin, D.Y. Salcedo, C.D. Rinc, Análisis de tensión/tamaño en compuestos ternarios AgIn5VI8 (VI = S, Se, Te) mediante difracción de Rayos-x, Rev. Mexic. Fisica 63 (2017) 345–350.

[36] Y.H. Zhao, Y.Z. Guo, Q. Wei, T.D. Topping, A.M. Dangelewicz, Y.T. Zhu, T. G. Langdon, E.J. Lavernia, Influence of specimen dimensions and strain measurement methods on tensile stress-strain curves, Mater. Sci. Eng. A. 525 (2009) 68–77, https://doi.org/10.1016/j.msea.2009.06.031.

[37] R.E. Stoller, S.J. Zinkle, On the relationship between uniaxial yield strength and resolved shear stress in polycrystalline materials, J. Nucl. Mater. 283–287 (2000) 349–352, https://doi.org/10.1016/S0022-3115(00)00378-0.

[38] M. Praud, F. Mompiou, J. Malaplate, D. Caillard, J. Garnier, A. Steckmeyer, B. Fournier, Study of the deformation mechanisms in a Fe–14% Cr ODS alloy, J. Nucl. Mater. 428 (2012) 90–97, https://doi.org/10.1016/J.JNUCMAT.2011.10.046.

[39] S. Ohtsuka, S. Ukai, M. Fujiwara, T. Kaito, T. Narita, Improvement of 9Cr-ODS martensitic steel properties by controlling excess oxygen and titanium contents, J. Nucl. Mater. (2004) 329–333, https://doi.org/10.1016/J.JNUCMAT.2004.04.043, 372–376.

[40] S. Ohtsuka, S. Ukai, M. Fujiwara, T. Kaito, T. Narita, Nano-structure control in ODS martensitic steels by means of selecting titanium and oxygen contents, in: J. Phys. Chem. Solids, Pergamon, 2005, pp. 571–575, https://doi.org/10.1016/j.jpcs.2004.06.033.
[41] X. Boulnat, D. Fabrègue, M. Perez, S. Urvoy, D. Hamon, Y. de Carlan, Assessment of consolidation of oxide dispersion strengthened ferritic steels by spark plasma sintering: from laboratory scale to industrial products, Powder Metall. 57 (2014) 204–211, https://doi.org/10.1179/1743290114Y.0000000091.
[42] I. Hilger, X. Boulnat, J. Hoffmann, C. Testani, F. Bergner, Y. De Carlan, F. Ferraro, A. Ulbricht, Fabrication and characterization of oxide dispersion strengthened (ODS) 14Cr steels consolidated by means of hot isostatic pressing, hot extrusion and spark plasma sintering, J. Nucl. Mater. 472 (2016) 206–214, https://doi.org/10.1016/j.jnucmat.2015.09.036.
[43] X. Boulnat, M. Perez, D. Fabregue, T. Douillard, M.H. Mathon, Y. De Carlan, Microstructure evolution in nano-reinforced ferritic steel processed by mechanical alloying and spark plasma sintering, Metall. Mater. Trans. A Phys. Metall. Mater. Sci. 45 (2014) 1485–1497, https://doi.org/10.1007/s11661-013-2107-y.
[44] C. Heintze, M. Hernández-Mayoral, A. Ulbricht, F. Bergner, A. Shariq, T. Weissgärber, H. Frielinghaus, Nanoscale characterization of ODS Fe-9%Cr model alloys compacted by spark plasma sintering, J. Nucl. Mater. 428 (2012) 139–146, https://doi.org/10.1016/j.jnucmat.2011.08.053.
[45] Z. Oksiuta, N. Baluc, Effect of mechanical alloying atmosphere on the microstructure and Charpy impact properties of an ODS ferritic steel, J. Nucl. Mater. (2009) 386–388, https://doi.org/10.1016/j.jnucmat.2008.12.148, 426–429.
[46] M.J. Alinger, G.R. Odette, D.T. Hoelzer, On the role of alloy composition and processing parameters in nanocluster formation and dispersion strengthening in nanostuctured ferritic alloys, Acta Mater. 57 (2009) 392–406, https://doi.org/10.1016/j.actamat.2008.09.025.
[47] R. Rahmanifard, H. Farhangi, A.J. Novinrooz, Effect of zirconium and tantalum on the microstructural characteristics of 12YWT ODS steel nanocomposite, J. Alloys Compd. 622 (2015) 948–952, https://doi.org/10.1016/j.jallcom.2014.11.018.
[48] H. Xu, Z. Lu, S. Ukai, N. Oono, C. Liu, Effects of annealing temperature on nanoscale particles in oxide dispersion strengthened Fe-15Cr alloy powders with Ti and Zr additions, J. Alloys Compd. 693 (2017) 177–187, https://doi.org/10.1016/j.jallcom.2016.09.133.
[49] S. Mohan, G. Kaur, B.K. Panigrahi, C. David, G. Amarendra, Effect of Zr and Al addition on nanocluster formation in oxide dispersion strengthened steel - an ab initio study, J. Alloys Compd. 767 (2018) 122–130, https://doi.org/10.1016/j.jallcom.2018.07.047.
[50] C.L. Fu, M. Krčmar, G.S. Painter, X.Q. Chen, Vacancy mechanism of high oxygen solubility and nucleation of stable oxygen-enriched clusters in Fe, Phys. Rev. Lett. 99 (2007) 1–4, https://doi.org/10.1103/PhysRevLett.99.225502.
[51] A. Claisse, P. Olsson, First-principles calculations of (Y, Ti, O) cluster formation in body centred cubic iron-chromium, Nucl. Instrum. Methods Phys. Res. Sect. B Beam Interact. Mater. Atoms 303 (2013) 18–22, https://doi.org/10.1016/j.nimb.2013.01.016.
[52] D. Murali, B.K. Panigrahi, M.C. Valsakumar, C.S. Sundar, Diffusion of y and Ti/Zr in bcc iron: a first principles study, J. Nucl. Mater. 419 (2011) 208–212, https://doi.org/10.1016/j.jnucmat.2011.05.018.
[53] D. Murali, B.K. Panigrahi, M.C. Valsakumar, S. Chandra, C.S. Sundar, B. Raj, The role of minor alloying elements on the stability and dispersion of yttria nanoclusters in nanostructured ferritic alloys: an ab initio study, J. Nucl. Mater. 403 (2010) 113–116, https://doi.org/10.1016/j.jnucmat.2010.06.008.
[54] Y. Jiang, J.R. Smith, G.R. Odette, Formation of Y-Ti-O nanoclusters in nanostructured ferritic alloys: a first-principles study, Phys. Rev. B - Condens. Matter Mater. Phys. 79 (2009) 1–7, https://doi.org/10.1103/PhysRevB.79.064103.
[55] I. Bogachev, E. Grigoryev, O.L. Khasanov, E. Olevsky, Fabrication of 13Cr-2Mo ferritic/martensitic oxide-dispersion-strengthened steel components by mechanical alloying and spark-plasma sintering, Jom 66 (2014) 1020–1026, https://doi.org/10.1007/s11837-014-0972-5.
[56] J. Trapp, B. Kieback, Temperature distribution in metallic powder particles during initial stage of field-activated sintering, J. Am. Ceram. Soc. 98 (2015) 3547–3552, https://doi.org/10.1111/jace.13757.
[57] X. Song, X. Liu, J. Zhang, Neck Formation and self-adjusting mechanism of neck growth of conducting powders in spark plasma sintering, J. Am. Ceram. Soc. 89 (2006) 494–500, https://doi.org/10.1111/j.1551-2916.2005.00777.x.
[58] S. Diouf, A. Molinari, Densification mechanisms in spark plasma sintering: effect of particle size and pressure, Powder Technol. 221 (2012) 220–227, https://doi.org/10.1016/j.powtec.2012.01.005.
[59] P. Franke, C. Heintze, F. Bergner, T. Weißgärber, Mechanical properties of spark plasma sintered Fe-Cr compacts strengthened by nanodispersed yttria particles, Mater. Test. 52 (2010) 133–138, https://doi.org/10.3139/120.110115.
[60] A.S. Semenov, J. Trapp, M. Nöthe, O. Eberhardt, T. Wallmersperger, B. Kieback, Experimental and numerical analysis of the initial stage of field-assisted sintering of metals, J. Mater. Sci. 52 (2017) 1486–1500, https://doi.org/10.1007/s10853-016-0444-0.
[61] X. Zhou, Y. Liu, L. Yu, Z. Ma, Q. Guo, Y. Huang, H. Li, Microstructure characteristic and mechanical property of transformable 9Cr-ODS steel fabricated by spark plasma sintering, Mater. Des. 132 (2017) 158–169, https://doi.org/10.1016/J.MATDES.2017.06.063.
[62] N. Kamikawa, K. Sato, G. Miyamoto, M. Murayama, N. Sekido, K. Tsuzaki, T. Furuhara, Stress–strain behavior of ferrite and bainite with nano-precipitation in low carbon steels, Acta Mater. 83 (2015) 383–396, https://doi.org/10.1016/J.ACTAMAT.2014.10.010.
[63] J. Shen, Y. Li, F. Li, H. Yang, Z. Zhao, S. Kano, Y. Matsukawa, Y. Satoh, H. Abe, Microstructural characterization and strengthening mechanisms of a 12Cr-ODS steel, Mater. Sci. Eng. A. 673 (2016) 624–632, https://doi.org/10.1016/j.msea.2016.07.030.
[64] M. Dadé, J. Malaplate, J. Garnier, F. De Geuser, F. Barcelo, P. Wident, A. Deschamps, Influence of microstructural parameters on the mechanical properties of oxide dispersion strengthened Fe-14Cr steels, Acta Mater. 127 (2017) 165–177, https://doi.org/10.1016/j.actamat.2017.01.026.
[65] X. Zhou, Y. Liu, L. Yu, Z. Ma, Q. Guo, Y. Huang, H. Li, Microstructure characteristic and mechanical property of transformable 9Cr-ODS steel fabricated by spark plasma sintering, Mater. Des. 132 (2017) 158–169, https://doi.org/10.1016/j.matdes.2017.06.063.